

Simulation of Coupled Unsteady Flow and Heat Conduction in Turbine Stage

Douglas L. Sondak*

Boston University, Boston, Massachusetts 02215

and

Daniel J. Dorney†

Virginia Commonwealth University, Richmond, Virginia 23284-3015

A three-dimensional, unsteady, compressible, finite difference Navier-Stokes solver has been coupled with a three-dimensional, unsteady, finite difference conduction heat-transfer solver to study conjugate heat-transfer problems in turbomachinery. The heat-transfer solver was validated by computing unsteady heat transfer in a cylinder and comparing the results with an analytical solution. The code was then applied to a high-pressure turbine stage, typical of those found in modern high-bypass turbofan engines, with a nonuniform inlet temperature profile. The unsteady temperature field of a rotor blade, both at the surface and within the blade, has been examined in detail. The surface-temperature results have also been compared with those from a flow simulation in which the blade surfaces were assumed to be adiabatic, demonstrating the need for the coupled approach.

Nomenclature

a	= speed of sound
$\hat{E}, \hat{F}, \hat{G}$	= fluxes, generalized coordinates
H	= height of cylinder
J	= Jacobian of coordinate transformation
J_0	= Bessel function of order zero of the first kind
J_1	= Bessel function of order one of the first kind
\hat{Q}	= conserved variable, generalized coordinates
R	= outer radius of cylinder
r, θ, z	= cylindrical coordinates
T	= temperature
T_s	= surface temperature
T_0	= initial temperature
t	= time
u	= axial velocity
V	= isentropic velocity
V_{cr}	= critical velocity
α	= diffusion coefficient
β_m	= m th root of J_0
γ	= ratio of specific heats
ξ, η, ζ	= generalized coordinates

Subscripts

t	= total
1	= inlet
2	= between vane and rotor
3	= exit

Introduction

THE design of high-pressure turbines requires compromise between the need for high inlet temperatures for good thermodynamic efficiency and low inlet temperatures for structural integrity and long life. Accurate unsteady temperature distributions within the

turbine vane and blade are difficult to predict, and so large safety margins must be employed to ensure that hot spots and thermal cycling do not damage the blades. Improved temperature predictions could lead to higher inlet temperatures and designs with improved turbine life.

To simulate conduction heat transfer within a turbine blade, the surface boundary condition must be specified. The surface temperature in an actual operating environment varies spatially and temporally because of unsteady interaction between adjacent blade rows, secondary flows, nonuniform inflow temperature fields, flow acceleration and deceleration, etc. Flowfields can be significantly affected by heat transfer to or from adjacent surfaces.¹ To accurately simulate blade heat transfer, it is therefore required to couple an unsteady flow solver with an unsteady conduction heat-transfer solver. The coupling of flow and conduction heat-transfer solutions is sometimes referred to as a conjugate heat-transfer problem.

Several studies are available in the literature in which conjugate heat-transfer problems have been solved for turbine blades. Li and Kassab² coupled an explicit, finite volume, Navier-Stokes solver with a boundary element method heat-conduction solver. They solved a two-dimensional, steady-state problem for flow and heat transfer in a turbine cascade. Simulations were performed assuming adiabatic blade surfaces as well as for the conjugate problem, and they found that the conjugate solution resulted in much cooler blade surfaces. Heselhaus and Vogel³ performed a three-dimensional steady-state simulation, also on a turbine cascade. They used an explicit, finite volume flow solver and a finite element heat-conduction solver. In comparing surface temperatures for the conjugate solution with those from an uncoupled solution, they found large differences. Kao and Liou⁴ solved the same two-dimensional, steady-state turbine cascade problem as Li and Kassab.² They used explicit, finite volume methods for both the flow and heat-transfer solutions, employing a structured grid for the flow and an unstructured grid for the heat conduction. Their results were similar to those of Li and Kassab,² showing much cooler surface temperatures using the conjugate method than with adiabatic walls. In all of these studies, the Baldwin-Lomax turbulence model⁵ was used.

None of the studies just noted addressed the *unsteadiness* of the temperature field in an actual turbine rotor environment. In the present study a three-dimensional, finite difference heat-conduction solver has been developed to compute the unsteady temperature field within a turbine blade, and it has been coupled with a three-dimensional, unsteady, compressible, finite difference Navier-Stokes solver. To verify the accuracy of the heat-conduction

Presented as Paper 99-2521 at the AIAA/ASME/SAE/ASEE Joint Propulsion Conference and Exhibit, Los Angeles, CA, 20-24 June 1999; received 24 June 1999; revision received 20 October 1999; accepted for publication 20 October 1999. Copyright © 1999 by the American Institute of Aeronautics and Astronautics, Inc. All rights reserved.

*Senior Scientific Programmer, Boston University, Office of Information Technology, 111 Cummington Street.

†Associate Professor, Department of Mechanical Engineering, 601 West Main Street, Room 318, P.O. Box 843015.

solver, the unsteady temperature distribution in a right circular cylinder with an impulsively imposed surface temperature has been computed, and the results have been compared to an analytical solution. The flow and heat transfer in a single-stage turbine with a nonuniform inlet temperature distribution was then computed, and the unsteady temperature field within a rotor blade was examined in detail.

Conduction Heat-Transfer Solver

Assuming that there are no heat sources or sinks within the blades, the heat equation is given by

$$\frac{\partial T}{\partial t} - \alpha \nabla^2 T = 0 \quad (1)$$

In generalized, curvilinear coordinates the equation is

$$\frac{\partial \hat{Q}}{\partial t} - \alpha \left(\frac{\partial \hat{E}}{\partial \xi} + \frac{\partial \hat{F}}{\partial \eta} + \frac{\partial \hat{G}}{\partial \zeta} \right) = 0 \quad (2)$$

where

$$\hat{Q} = J^{-1} T \quad (3)$$

Neglecting cross-derivative terms, \hat{E} , \hat{F} , and \hat{G} are given by

$$\hat{H} = J^{-1} (\phi_x^2 + \phi_y^2 + \phi_z^2) T_\phi \quad (4)$$

where \hat{H} represents \hat{E} , \hat{F} , or \hat{G} and ϕ represents ξ , η , or ζ , respectively. Here, subscripts represent partial differentiation.

Linearizing, discretizing in time, and applying approximate factorization results in the equation

$$\begin{aligned} & [I - \alpha \Delta t \partial_\xi J^{-1} (\xi_x^2 + \xi_y^2 + \xi_z^2) \partial_\xi J] [I - \alpha \Delta t \partial_\eta J^{-1} (\eta_x^2 + \eta_y^2 \\ & + \eta_z^2) \partial_\eta J] [I - \alpha \Delta t \partial_\zeta J^{-1} (\zeta_x^2 + \zeta_y^2 + \zeta_z^2) \partial_\zeta J] \Delta \hat{Q} \\ & = \alpha \Delta t (\partial_\xi \hat{E} + \partial_\eta \hat{F} + \partial_\zeta \hat{G}) \end{aligned} \quad (5)$$

The conduction heat transfer was solved on collapsed O grids as shown for a midspan cut in Fig. 1. The grid was clustered at the surface because that is where the greatest temperature unsteadiness was expected. Equation (5) was solved implicitly using a tridiagonal solver for nonperiodic coordinate directions and a periodic tridiagonal solver for periodic coordinate directions.

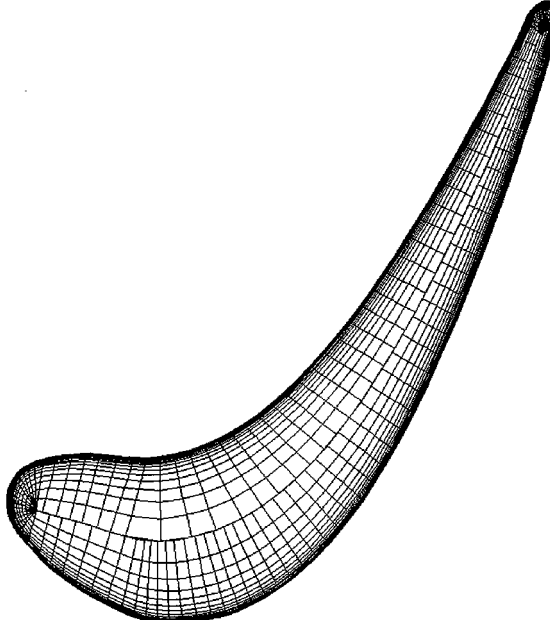


Fig. 1 Midspan section of rotor heat-conduction grid.

Flow Solver

The three-dimensional, Reynolds-averaged, unsteady, Navier-Stokes equations were solved using an implicit, time-marching, finite difference scheme.⁶ The inviscid fluxes were discretized using Roe's scheme,⁷ and viscous fluxes were discretized using standard central differences. The Baldwin-Lomax⁵ algebraic turbulence model was used for turbulence closure. The procedure is second-order accurate in time and third-order accurate in space. The equations were solved using approximate factorization and a block tridiagonal solver.

Each blade passage was modeled with an O grid around the airfoil, overset on an H grid, which fills the remainder of the passage, as shown in Fig. 2. This technique permits good resolution in the leading- and trailing-edge regions and allows the application of periodic boundary conditions in the blade-to-blade direction without interpolation. The flow variables at zonal boundaries between the O grid and H grid were explicitly updated after each time step by interpolating values from the adjacent grid. Grid lines at the blade surface were coincident between the conduction and flow grids so that no interpolation was required at the interface.

Cylinder Test Case

To test the heat-conduction solver, the unsteady heat transfer in a right circular cylinder was computed numerically and analytically. The height of the cylinder was set to a value of 1.0, where lengths are nondimensionalized by the cylinder radius. A $41 \times 21 \times 21$ grid (circumferential, radial, and spanwise, respectively), uniform in each coordinate direction, was used for the numerical computation. The surface grid is shown in Fig. 3.

The temperature of the cylinder was initialized to a value of 1. The wall temperature, including the top and bottom of the cylinder, was impulsively changed to a value of 2 at $t = 0$ and held at that value for $t > 0$. For the numerical solution periodicity was enforced in the circumferential direction, and the temperature at the centerline

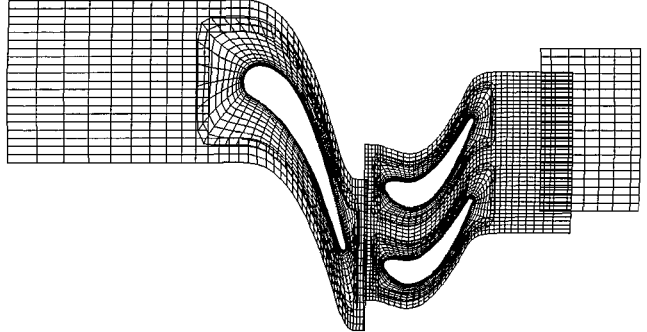


Fig. 2 Midspan section of flow grid, every other grid line.

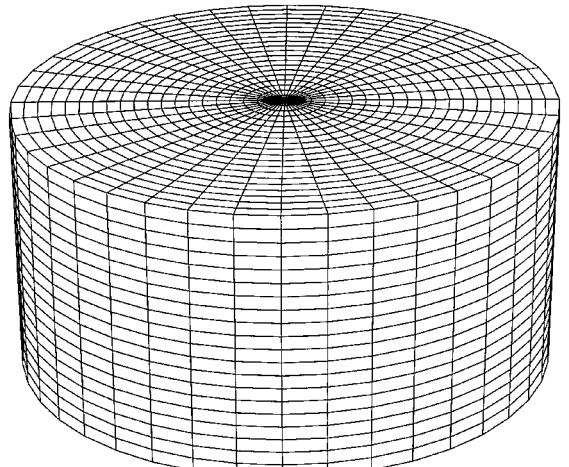


Fig. 3 Cylinder surface grid.

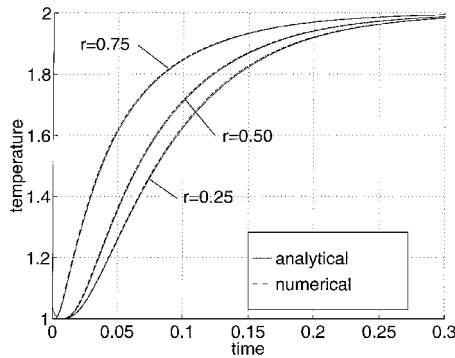


Fig. 4 Temperature history, cylinder test case, height = 0.5.

of the cylinder, $j = 1$, was set to the circumferential average of the temperature at $j = 2$. The heat diffusion coefficient α was set to a value of 1.

For the analytical solution the equation was cast in cylindrical coordinates. Assuming circumferential symmetry, $T(r, z, t)$ is given by

$$\frac{\partial T}{\partial t} - \alpha \left(\frac{\partial^2 T}{\partial r^2} + \frac{1}{r} \frac{\partial T}{\partial r} + \frac{\partial^2 T}{\partial z^2} \right) = 0 \quad (6)$$

with boundary conditions

$$T(R, z, t) = T_s, \quad 0 < t < \infty \quad (7)$$

$$T(r, 0, t) = T_s, \quad 0 < t < \infty \quad (8)$$

$$T(r, H, t) = T_s, \quad 0 < t < \infty \quad (9)$$

and initial condition

$$T(r, z, t) = T_0, \quad t = 0 \quad (10)$$

where R is the outer radius and H is the height of the cylinder.

The analytical solution of Eqs. (6–10) can be expressed as an infinite series using Bessel functions of the first kind,⁸

$$T(r, z, t) = T_s + \frac{4T_0}{\pi} \sum_{k=1}^{\infty} \sum_{m=1}^{\infty} \frac{1 - \cos k\pi}{k\beta_m J_1(\beta_m)} \times \exp[-\alpha(\beta_m^2 + k^2\pi^2)t] J_0(\beta_m r) \sin k\pi z \quad (11)$$

The results of the computation at a height of 0.5 and radii of 0.25, 0.50, and 0.75 are compared to the analytical solution in Fig. 4. The match between the analytical and numerical solutions is excellent.

Turbine Simulation

The turbine configuration in the present study is based on experiments performed at NASA Lewis Research Center.^{9–11} The purpose of the experiments was to investigate the effects of nonuniform turbine inlet temperature profiles on turbine performance. The turbine was typical of high-pressure turbines in high-bypass turbofan engines. It operated in the high subsonic regime, with a peak Mach number of approximately 0.92. In the experiment cool air was injected through circumferential slots in the hub and tip end walls near the inlet, resulting in nonuniform radial total temperature and total pressure distributions. Note that the rotor-blade temperatures were not measured in the experiment; this configuration was chosen for the present study as a realistic high-speed turbine geometry.

In the experiment the inlet total temperature profile was uniform circumferentially. In actual engines combustor hot streaks cause radial and circumferential variations in temperature.¹² In the present study a circular hot streak was superimposed on the experimental temperature profile to simulate such a temperature field. The hot streak had a hyperbolic tangent profile and was centered at 40% span, similar to that investigated by Butler et al.¹³ The radial inlet

Table 1 Operating conditions

Parameter	Value
Avg. T_{t1}	672.2 K
Avg. P_{t1}	3.103×10^5 Pa
Mass flow	6.130 kg/s
Specific work	1.229×10^5 J/kg
Rotational speed	11,373 RPM
P_{t3}/P_{t1}	2.360

Table 2 Grid dimensions (1,360,629 total points)

Grid	Vane	Each rotor blade	Exit duct
O ^a	121 × 31 × 51	121 × 31 × 51	—
H ^b	86 × 41 × 51	85 × 41 × 51	14 × 41 × 51
C ^c	—	121 × 18 × 51	—
Total	371,127	480,114	29,274

^aO grid. ^bH grid. ^cConduction grid.

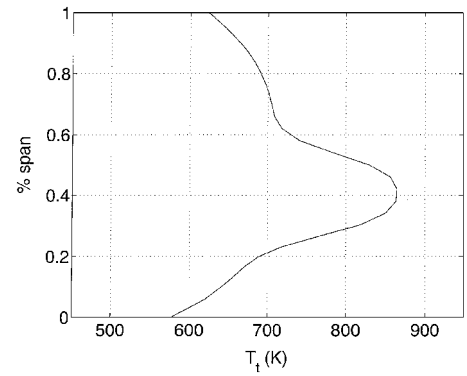


Fig. 5 Inlet total temperature profile.

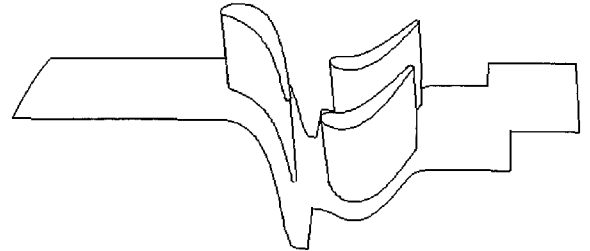


Fig. 6 Computational domain.

total temperature profile through the center of the hot streak is shown in Fig. 5. The operating conditions are shown in Table 1.

The experimental configuration had 26 vanes and 48 rotor blades. To reduce the cost of the three-dimensional computation, the number of vanes in the first row was decreased to 24, and the dimensions of the vane airfoil sections were increased by a factor of $\frac{26}{24}$ to maintain the same blockage, resulting in a 1–2 airfoil count ratio in the simulation. Tip clearance was not modeled, with the rotor tip scraping along the tip flowpath, because the tip-clearance flow is not of primary importance in the present study. A line drawing of the full computational domain, showing the hub flowpath but not the tip flowpath (for clarity), is shown in Fig. 6. The flowpath is in three distinct sections because the flowpath under the rotor blades rotates with the blades, whereas the flowpath under the vanes and downstream of the rotor is stationary. The midspan section of the flow grid, with every other grid line deleted for clarity, is shown in Fig. 2, and the conduction grid is shown in Fig. 1. Heat conduction was computed in both rotor blades (but not in the vane). Grid dimensions for the entire domain are shown in Table 2. These grids resulted in an average $y^+ = 3$ at the rotor surface.

Characteristic boundary conditions were used at the inflow and outflow boundaries. At the inflow boundary, total pressure, total

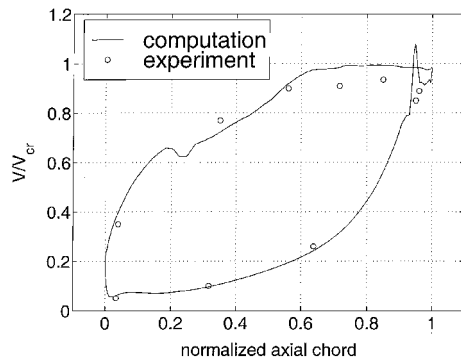


Fig. 7 Vane midspan isentropic velocity profile, adiabatic blade surfaces.

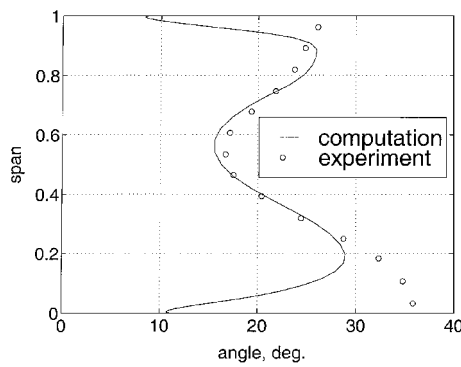


Fig. 8 Stage exit flow angle, adiabatic blade surfaces.

temperature, and the radial and circumferential velocity components were specified, and the streamwise derivative of the upstream running Riemann invariant $R_2 = u - 2a/(\gamma - 1)$ was set to zero. At the outflow boundary the streamwise derivative of the radial and circumferential velocity components, entropy, and the downstream running Riemann invariant were set to zero. The ratio of midspan outflow static pressure to inlet total pressure was specified as 0.3855, the experimental value. Static pressures at other outflow radial locations were obtained from the radial equilibrium equation. Periodicity was enforced in the circumferential direction. On airfoil surfaces the no-slip boundary condition was employed, and the normal derivative of pressure was set to zero. The vane surface was assumed to be adiabatic.

In a companion study¹⁴ simulations of the present configuration were performed at the experimental operating condition with the assumption of adiabatic rotor blade surfaces. Comparisons of vane midspan isentropic velocity profile and stage exit flow angle with experimental data are shown in Figs. 7 and 8. The computation is in reasonably good agreement with the data except for the flow angle near the hub. This discrepancy is caused by differences in secondary flow, attributable to the turbulence model employed here. In a three-dimensional, steady-state, Navier-Stokes simulation of the current configuration, Kim and Stubbs¹⁵ also showed a discrepancy in predicted flow angle near the hub, though in the opposite direction.

Flow/Heat-Conduction Coupling

Typical values of rotor-blade thermal conductivity and thermal diffusivity were chosen: 17.3 W/m-K (10 Btu/hr-ft-°R) and 6.3×10^{-7} m²/s (6.8×10^{-6} ft²/s), respectively. In the conduction solver the end walls were assumed to be adiabatic, and the blade surface temperature was determined from the flow solution as described next. Note that the O grid collapses to a line at the blade's camber line, and a number of grid lines collapse to points near the leading and trailing edges. The method used to set the boundary condition at the collapsed grid line of each blade section will be described in reference to Fig. 9, which is a close-up diagram of the collapsed line ($j = 1$) and the adjacent grid line ($j = 2$).

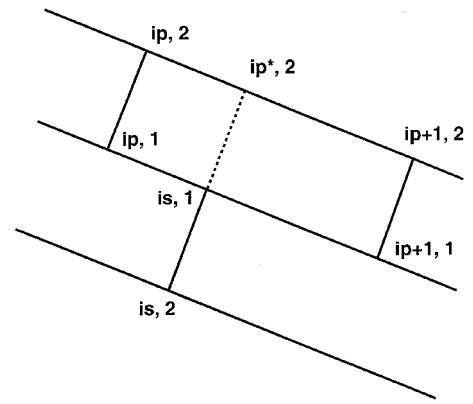


Fig. 9 Diagram of collapsed grid line at camber line of blade section.

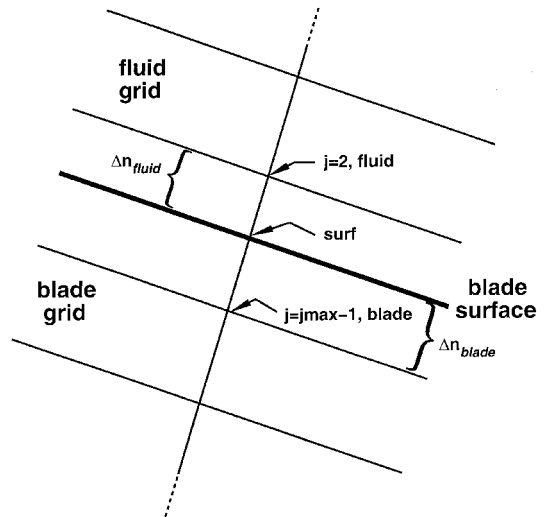


Fig. 10 Diagram of interface between fluid and conduction grids.

example the boundary condition will be set for a grid line on the suction-surface (lower) side of the blade. The i index of the grid line is "is," and the point at which the boundary condition will be calculated is (is, 1) because the collapsed grid line is at ($j = 1$). The two points on the pressure-surface side of the blade that straddle point (is, 1) are labeled (ip, 1) and (ip + 1, 1). The grid line (is = const) is extended toward the pressure side of the blade as shown by the dashed line. The temperature at the point of intersection of this line with the ($j = 2$) grid line, designated (ip*, 2) in the figure, is computed by linearly interpolating between (ip, 2) and (ip + 1, 2). The temperature at the required point (is, 1) is then computed by linearly interpolating between (ip*, 2) and (is, 2).

For the grid lines that collapse to a point, the temperature at ($j = 2$) is averaged, and the average temperature is applied to the collapsed point at ($j = 1$).

A diagram of the interface between the fluid and heat conduction grids is shown in Fig. 10. The heat-transfer rate at the surface must be identical in the fluid and in the blade,

$$k_{\text{fluid}} \left. \frac{\partial T}{\partial n} \right|_{\text{fluid}} = k_{\text{blade}} \left. \frac{\partial T}{\partial n} \right|_{\text{blade}} \quad (12)$$

or in terms of finite differences,

$$k_{\text{fluid}} \left(\frac{T_{j=2,\text{fluid}}^{(n+1)*} - T_{\text{surf}}^n}{\Delta n_{\text{fluid}}} \right) \approx k_{\text{blade}} \left(\frac{T_{\text{surf}}^{(n+1)} - T_{j=j \max-1,\text{blade}}^n}{\Delta n_{\text{blade}}} \right) \quad (13)$$

where $(n+1)^*$ indicates that the fluid solution (but not the heat conduction solution) has been advanced to time level $(n+1)$. Equation (13) was solved for $[T_{\text{surf}}^{(n+1)}]$, and this was the boundary condition for the conduction step at time level $(n+1)$.

The flow solution was first performed with adiabatic rotor blade surfaces. The rotor blades were then initialized to an arbitrary value of 556 K (1000°R). The rotor-blade surface-temperature distribution was computed from the flow solution, and the blade surface was impulsively changed to this temperature field. The flowfield was frozen, and the heat-conduction solver was marched in time until the l_∞ norm of the temperature changes dropped by two orders of magnitude. This defined the initial condition for the coupled flow/heat-conduction solution. The coupled system was then iterated for an additional four cycles, where a cycle is defined as the

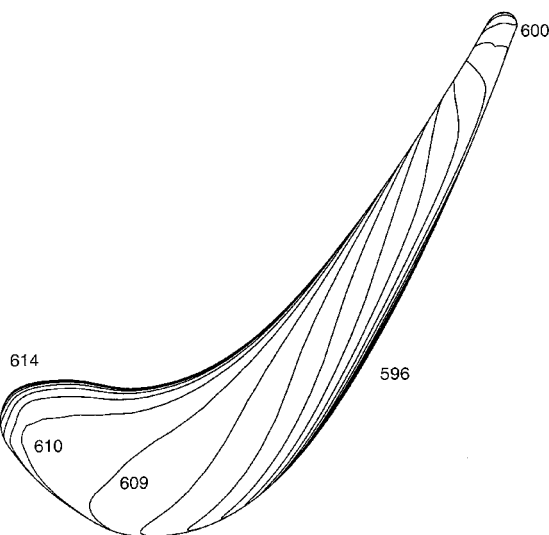


Fig. 11 Instantaneous temperature (K) within rotor blade at midspan.

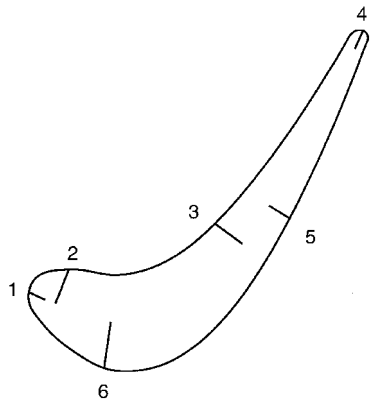


Fig. 12 Numerical rotor temperature tap locations, midspan.

time required for the two rotor blades to traverse the single vane, to ensure periodicity.

A time step was chosen such that there were 12,000 steps per cycle. Because there are two rotor blades for each vane, that is a resolution of 6000 steps per blade passing. This is sufficient to resolve unsteadiness at the blade-passing frequency as well as higher frequencies such as those caused by vortex shedding.¹⁶ To ensure that this time step was also adequate for the conduction solver, the turbine-blade material properties were applied to the analytical solution for heat conduction in a cylinder that was just presented. Based on a 20 K difference between the initial and surface temperatures, which is of the order of the maximum unsteady temperature variation in the turbine simulation, the time required for a 0.1 K temperature change at 90% radius was orders of magnitude greater than the time step based on 12,000 steps per cycle. The timescale for the flow was therefore much smaller than that for the heat transfer, and so the flow-based time step was used.

The heat-conduction solver was found to have a more stringent stability limit than the flow solver. The least stable regions of the conduction grid were near the leading and trailing edges where the constant i grid lines collapse to a point (Fig. 1). For each flow time step 20 subiterations were performed in the conduction solver, each with a time step equal to $0.05 * \Delta t_{\text{flow}}$. The coupled simulation required approximately 51 s per step running on four processors of an SGI Origin2000 with 195-MHz R10000 processors.

Results of Coupled Simulation

Figure 11 shows an instantaneous temperature field within the rotor blade at midspan. Contours are in increments of 1 K, with several contours labeled in the figure. The blade is hottest near the leading edge, where it interacts with the hot streak, and is coolest on the suction surface.

The unsteady temperature response was examined at 240 locations within one rotor blade. Because of space limitations, the presentation of results will be limited to 6 selected locations around the blade at two spanwise cuts. The six locations are shown for the midspan cut in Fig. 12. Along each line shown in the figure, temperature response will be shown at four depths within the blade, where depth is the fractional distance from the blade surface along the line. For taps 2, 3, 5, and 6, this is the fractional distance from the surface to the camber line. The spanwise cuts are at 30 and 50% span.

Before examining the temperature response curves, it will be useful to look at an instantaneous static temperature field entering the rotor. This is shown in Fig. 13 at a location 0.1 axial chord upstream of the rotor. The contour plot contains circumferential lines at 30, 50, and 70% span. The first two of these lines represent the radial locations of the temperature response curves. The hot streak can be seen just above midspan on the left side of the plot. It has become elongated and skewed and has penetrated the layer of cooler air near the hub.

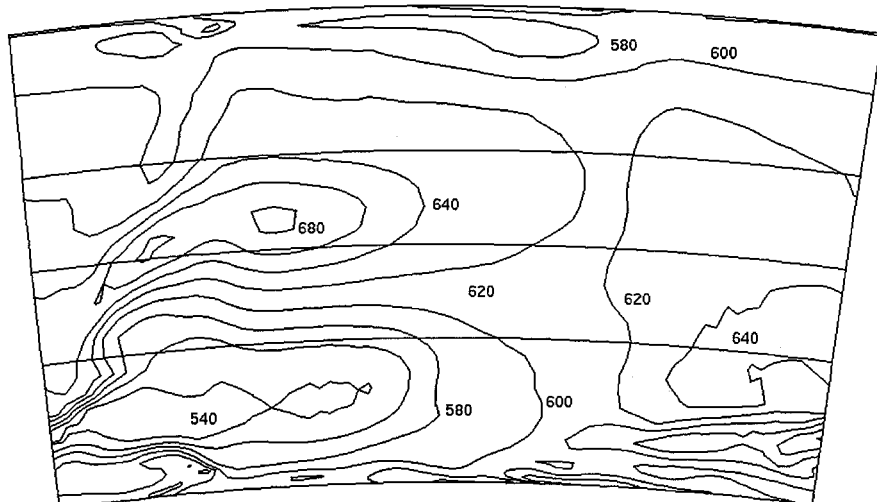


Fig. 13 Instantaneous static temperature (K), 0.1 axial chord upstream of rotor.

Convergence was ascertained by examining surface temperature traces over two cycles. Two of these traces at midspan, one on the rotor pressure surface at approximately 25% chord and one on the rotor suction surface at approximately 50% chord, are shown in Figs. 14 and 15. Small differences between cycles are caused by unsteadiness at frequencies other than blade-passing frequency caused by phenomena such as vortex shedding.

The temperature response curves are shown in Figs. 16–27. The temperature range is fixed at 25 K in each figure, but the minimum and maximum temperature shown may vary between figures.

Figure 16 shows the temperature response at the leading edge at 30% span. The surface temperature varies by 18 K (32°R) over the cycle caused by the rotor blade interacting with the edge of the hot streak. The temperature variation propagates through the blade thickness, with 3 K (5°R) variation at 100% depth. There are phase differences between the traces at different depths, with a phase difference of approximately 0.3 cycle between the surface and the 100% depth points. The maximum-depth point is hotter than the surface over 60% of the cycle. Just beyond the leading edge on the pressure surface, the response is similar to that at the leading edge, as shown in Fig. 17, but with smaller temperature variations.

Further downstream on the pressure surface there is a modest amount of activity, as shown in Fig. 18. The maximum-depth point

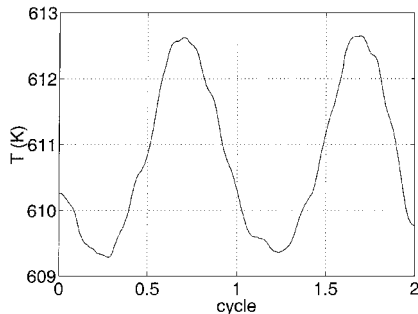


Fig. 14 Surface temperature response over two cycles, pressure surface, 50% span, 25% chord.

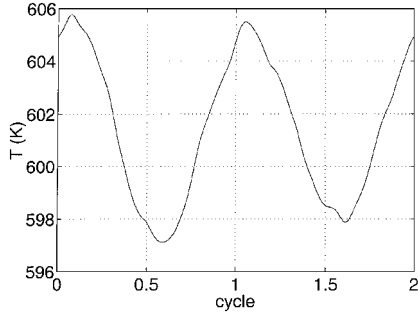


Fig. 15 Surface temperature response over two cycles, suction surface, 50% span, 50% chord.

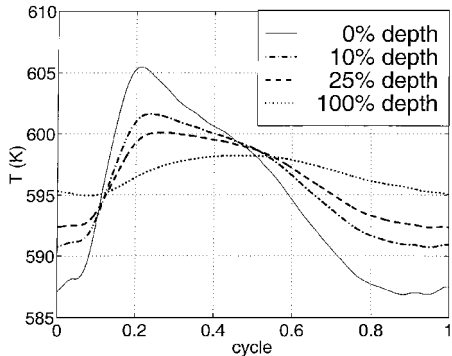


Fig. 16 Temperature response, 30% span, tap 1.

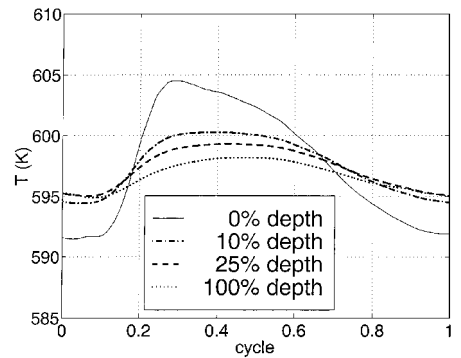


Fig. 17 Temperature response, 30% span, tap 2.

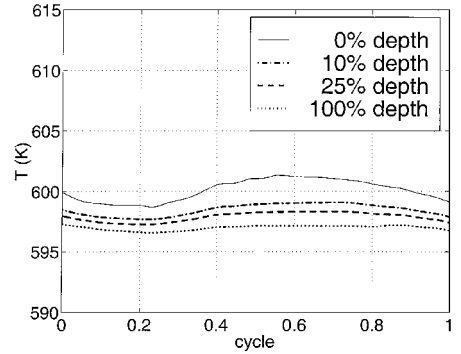


Fig. 18 Temperature response, 30% span, tap 3.

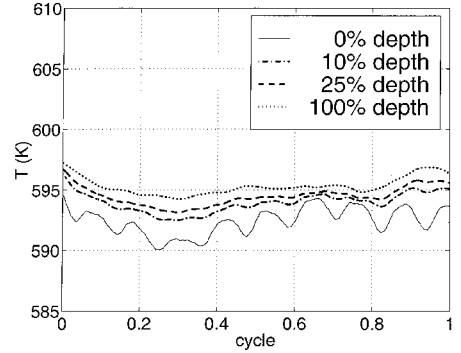


Fig. 19 Temperature response, 30% span, tap 4.

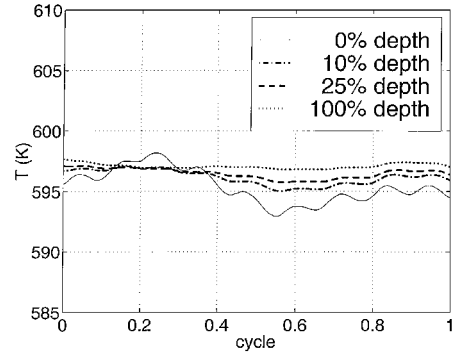


Fig. 20 Temperature response, 30% span, tap 5.

is nearly at a constant temperature and is always cooler than the surface.

The temperature response at the trailing edge is shown in Fig. 19. The high-frequency variation in the surface temperature is caused by vortex shedding. A similar variation may be seen on the suction surface at tap 5, as shown in Fig. 20.

At tap 6, shown in Fig. 21, most of the activity is at the surface, where the temperature variation is nearly 10 K (18°R).

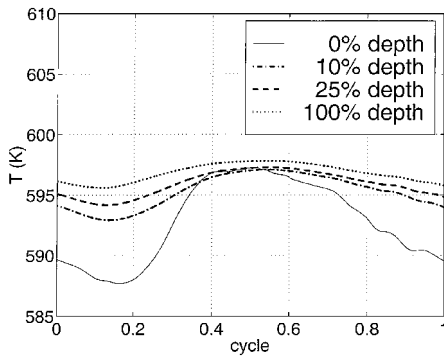


Fig. 21 Temperature response, 30% span, tap 6.

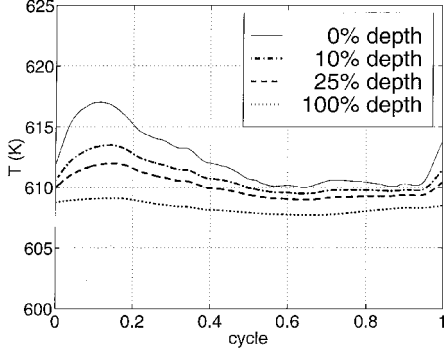


Fig. 22 Temperature response, 50% span, tap 1.

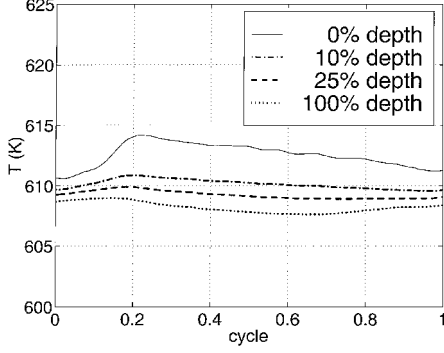


Fig. 23 Temperature response, 50% span, tap 2.

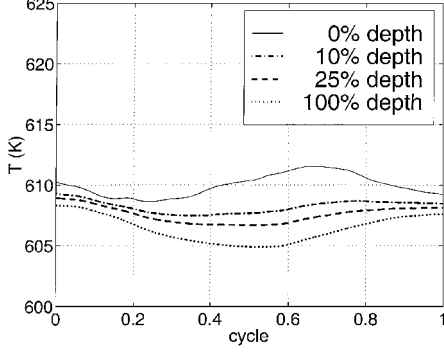


Fig. 24 Temperature response, 50% span, tap 3.

The temperature response at midspan is shown in Figs. 22–27. There is less activity in general than at 30% span (except for tap 5) because the circumferential temperature gradients are smaller, as seen in Fig. 13. At some locations, such as at tap 6 (Fig. 27), there is little temporal or spatial temperature variation.

Blade surface temperatures are compared between the simulation with adiabatic surfaces and that with heat conduction in Figs. 28–30 at 3 selected locations. Figure 28 shows the response at 30% span, tap 1 (leading edge). Both curves have a similar shape, but

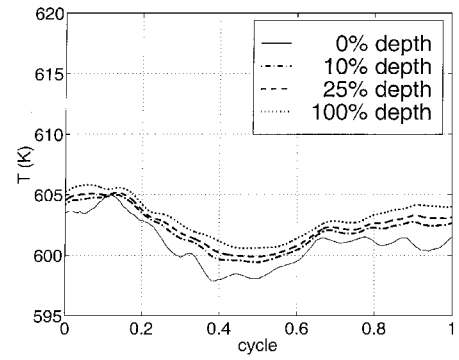


Fig. 25 Temperature response, 50% span, tap 4.

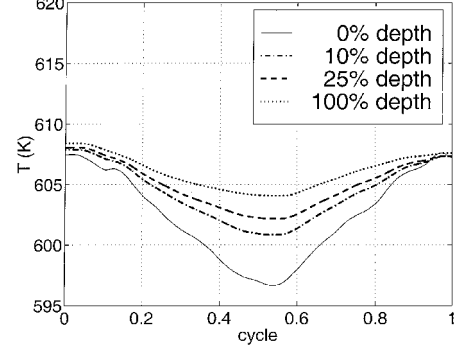


Fig. 26 Temperature response, 50% span, tap 5.

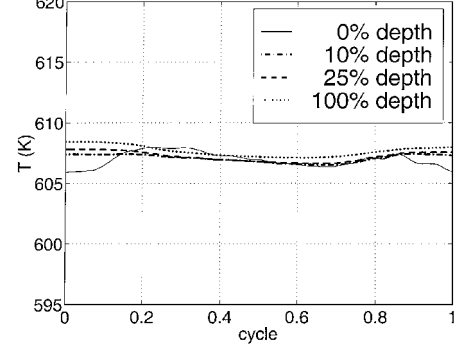


Fig. 27 Temperature response, 50% span, tap 6.

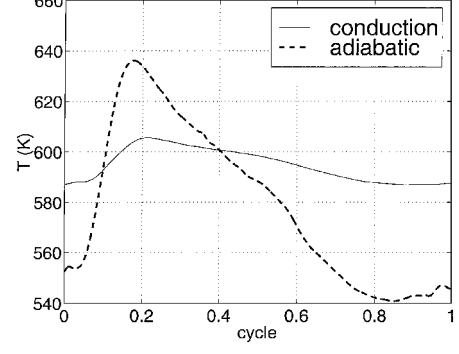


Fig. 28 Temperature response, 30% span, tap 1, adiabatic vs heat conduction.

heat conduction has a large damping effect on the surface temperature. The temperature varies by 95 K (171°R) for the adiabatic case, and it varies by 18 K (32°R) with heat conduction. The damping effect is also quite strong at 30% span, tap 4 (trailing edge) as shown in Fig. 29. The temperature variation caused by vortex shedding for the conduction case is a small fraction of that for the adiabatic wall case. The time-averaged surface temperature at this point is higher with the heat-conduction model. This contrasts

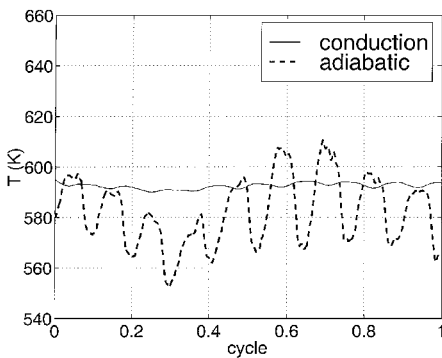


Fig. 29 Temperature response, 30% span, tap 4, adiabatic vs heat conduction.

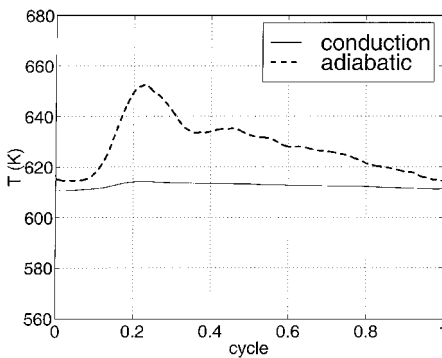


Fig. 30 Temperature response, 50% span, tap 2, adiabatic vs heat conduction.

the two-dimensional, steady-state studies of Li and Kassab² and Kao and Liou,⁴ where the heat-conduction models yielded lower wall temperatures than the adiabatic cases at all locations on the blades.

Figure 30 shows the response at 50% span, tap 2 (just downstream of the leading edge on the pressure surface). At this location the conduction case shows lower temperatures than the adiabatic case at all times. The time-averaged temperature is 612.6 K (1103°R) with conduction and 628.5 K (1131°R) for the adiabatic case.

Conclusions

1) It has been demonstrated that a coupled Navier-Stokes/heat-conduction solver is an effective means to compute the unsteady temperature field within a turbine blade.

2) Modeling heat conduction within the blades results in significantly less temporal surface temperature variation and different time-averaged surface temperatures than assuming that the blade surfaces are adiabatic.

3) Vortex shedding has been observed to cause high-frequency surface temperature variation at the trailing edge. For the current configuration the amplitude was approximately 2 K.

4) Even though an implicit solver was used, a significant time-step constraint was encountered at collapsed grid lines in the conduction grid. This needs to be investigated further and could be alleviated by a different grid configuration.

Acknowledgment

The authors would like to thank Boston University for providing the computer time for this study.

References

- Abeloff, P. A., Van Dalsem, W. R., and Dougherty, F. C., "Thermal Interaction Between an Impinging Hot Jet and a Conducting Solid Surface," AIAA Paper 90-3010, Aug. 1990.
- Li, H., and Kassab, A. J., "Numerical Prediction of Fluid Flow and Heat Transfer in Turbine Blades with Internal Cooling," AIAA Paper 94-2933, June 1994.
- Heselhaus, A., and Vogel, D. T., "Numerical Simulation of Turbine Blade Cooling with Respect to Blade Heat Conduction and Inlet Temperature Profiles," AIAA Paper 95-3041, July 1995.
- Kao, K.-H., and Liou, M.-S., "Application of Chimera/Unstructured Hybrid Grids for Conjugate Heat Transfer," *AIAA Journal*, Vol. 35, No. 9, 1997, pp. 1472-1478.
- Baldwin, B. S., and Lomax, H., "Thin Layer Approximation and Algebraic Model for Separated Turbulent Flows," AIAA Paper 78-257, Jan. 1978.
- Dorney, D. J., Davis, R. L., Edwards, D. E., and Madavan, N. K., "Unsteady Analysis of Hot Streak Migration in a Turbine Stage," *Journal of Propulsion and Power*, Vol. 8, No. 2, 1992, pp. 520-529.
- Roe, P. L., "Approximate Riemann Solvers, Parameter Vectors, and Difference Schemes," *Journal of Computational Physics*, Vol. 43, No. 2, 1981, pp. 357-372.
- Berg, P. W., and McGregor, J. L., *Elementary Partial Differential Equations*, Holden-Day, San Francisco, 1966, pp. 380-384.
- Whitney, W. J., Stabe, R. G., and Moffitt, T. P., "Description of the Warm Core Turbine Facility and the Warm Annular Cascade Facility Recently Installed at NASA Lewis Research Center," NASA TM 81562, Oct. 1980.
- Schwab, J. R., Stabe, R. G., and Whitney, W. J., "Analytical and Experimental Study of Flow Through an Axial Turbine Stage with a Nonuniform Inlet Radial Temperature Profile," AIAA Paper 83-1175, June 1983.
- Stabe, R. G., Whitney, W. J., and Moffitt, T. P., "Performance of a High-Work Low Aspect Ratio Turbine Tested with a Realistic Inlet Radial Temperature Profile," AIAA Paper 84-1161, June 1984.
- Dorney, D. J., Gundy-Burlet, K. L., and Sondak, D. L., "A Survey of Hot Streak Experiments and Simulations," *International Journal of Turbo and Jet Engines*, Vol. 16, No. 1, 1999, pp. 1-15.
- Butler, T. L., Sharma, O. P., Joslyn, H. D., and Dring, R. P., "Redistribution of an Inlet Temperature Distortion in an Axial Flow Turbine Stage," *Journal of Propulsion and Power*, Vol. 5, No. 1, 1989, pp. 64-71.
- Dorney, D. J., Sondak, D. L., and Cizmas, P. G. A., "Effects of Hot Streak/Airfoil Count Ratios in a High-Subsonic Single-Stage Turbine," AIAA Paper 99-2384, June 1999.
- Kim, S. C., and Stubbs, R. M., "Numerical Study of a High-Work Low-Aspect-Ratio Turbine Stage," AIAA Paper 95-3043, July 1995.
- Sondak, D. L., and Dorney, D. J., "Simulation of Vortex Shedding in a Turbine Stage," *Journal of Turbomachinery*, Vol. 121, No. 3, 1999, pp. 428-435.